Article

Not peer-reviewed version

Axial Stiffness Augmentation by Adding HTS Bulks or Limiting PM Rings to a Horizontal Axis HTS ZFC Radial Passive Bearing

António J. Arsénio Costa * , João F. P. Fernandes , Paulo J. Costa Branco

Posted Date: 17 April 2024

doi: 10.20944/preprints202404.1129.v1

Keywords: Zero-field cooling; High-temperature superconducting bulks; Passive magnetic bearing; Levitation; Guidance; Impulsion; Limiting PM rings; Axial stiffness; High-precision axial stability.

Article

Axial Stiffness Augmentation by Adding HTS Bulks or Limiting PM Rings to a Horizontal Axis HTS ZFC Radial Passive Bearing

António J. Arsénio Costa [1,*], João F. P. Fernandes [1,2] and Paulo J. Costa Branco [1,2]

[1] Instituto de Engenharia Mecânica (IDMEC), Laboratório Associado de Energia Transportes e Aeronáutica (LAETA), Av. Rovisco Pais, 1, 1049-001 Lisboa, Portugal
[2] IDMEC, Instituto Superior Técnico (IST), Universidade Lisboa (UL), Av. Rovisco Pais, 1, 1049-001 Lisboa, Portugal
* Correspondence: antoniojcosta@tecnico.ulisboa.pt

Abstract: This paper analyses the viability of different solutions to passively augment the axial stiffness of a horizontal axis radial levitation passive magnetic bearing (PMB) with topology previously studied. The zero-field cooling (ZFC) of high-temperature superconductor (HTS) bulks promotes higher magnetic impulsion and levitation forces and lower electromagnetic losses than with the field-cooling (FC), but on the other hand, the guiding stability is much lower than with FC. Because of stability reasons, FC was adopted in most superconducting maglev systems. The trend of this research group has been to develop a horizontal axis HTS ZFC radial levitation PMB presenting notable levitation forces with reduced electromagnetic losses, defined by a topology that creates guiding stability. Previous work has shown that even optimizing the bearing geometry to maximize magnetic guidance forces, could not be enough to guarantee the axial stiffness required for many applications. First, the extent to which guidance forces are augmented by increasing the number of HTS bulks in the stator is evaluated. Then, the axial stiffness augmentation by passively adding two limiting permanent magnet (PM) rings is evaluated. Results show that, the axial stiffness is highly augmented by adding limiting PM rings with no significant additional investment. This change enables using the studied ZFC superconducting PMB in high-precision axial stability applications, such as precision gyroscopes, horizontal axis propellers and turbines.

Keywords: zero-field cooling; high-temperature superconducting bulks; passive magnetic bearing; levitation; guidance; impulsion; limiting PM rings; axial stiffness; high-precision axial stability

1. Introduction

This paper studies different techniques to improve the axial stiffness of a known horizontal axis high-temperature superconducting (HTS) zero-field cooled (ZFC) horizontal axis radial levitation bearing. The enhancement of axial stiffness is tested by passively adding limiting permanent magnet (PM) rings aligned with the PM rotor and independent from the PM rotor at a specific distance from the side rotor PM rings. With this new not significant cost addition, the modified bearing may compete in terms of guiding stability with field-cooled (FC) superconducting magnetic bearings (SMB) for high-precision axial stability applications such as precision gyroscopes, horizontal axis propellers, and turbines. The focus of adopting ZFC instead of FC is to get higher impulsion and levitation forces, allowing an increase in the gap and safety distance [1,2] and reducing the magnetic field penetration and electromagnetics losses in HTS bulks, increasing efficiency [3,4] and extending their lifetime [5,6].

Figures 1(a) and 1(b) show respectively a photo and the 3D design of the known HTS ZFC bearing experimental prototype assembly. Figure 1(c) shows the 3D design of the experimental prototype extrusion.

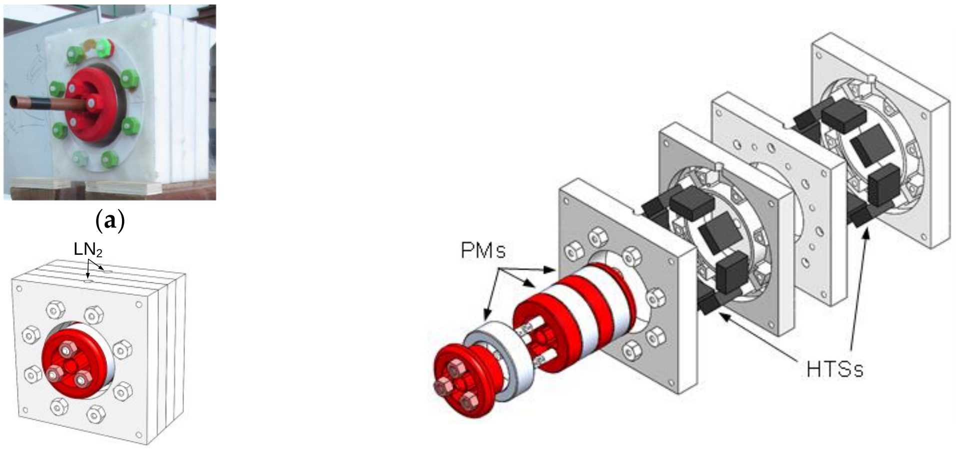

(**a**) (**b**) (**c**)

Figure 1. A photo (a), the assembly 3D design (b), and the extruded 3D design (c) of the studied HTS ZFC passive magnetic bearing experimental prototype.

The studied passive bearing geometry includes a stator housing two discontinuous rings of HTS bulks cryocooled using ZFC, and a PM rotor including three radially magnetized PM rings disposed in an alternate polarization arrangement. Each discontinuous ring of HTS bulks in the stator could contain a maximum of eight HTS bulks. The polarization of the intermediate PM ring is opposite from the polarizations of the two side PM rings, existing attraction between adjacent PM rings in the rotor [7].

The initial prediction of magnetic levitation and guidance forces and measurement of rotor dynamics were performed in [7]. Studies on the LN2 consumption and YBCO bulk temperature evolution for different thermal processes in the initial ZFC and the operation of the experimental bearing prototype were presented [8,9]. A methodology was developed to predict the released thermal power evolution from the measured LN2 mass loss rate used to determine the autonomous safety service time of the studied horizontal HTS ZFC levitating bearing [10]. Initial optimization of the bearing geometry volume and cost with maximization of levitation forces was performed [11]. Additional optimization of the PM ring and HTS bulk ring spacings was done to maximize the bearing guiding stability [12].

A method to measure the stiffness of a repulsive PMB in single gimbal magnetically suspended control moment gyroscope was proposed [13]. A model was developed to determine the magnetic stiffness in radial flux permanent magnet generators of direct-drive wind turbines from the structural mechanical stiffness depending on the verified operation deflection [14]. An axial flux high-temperature superconducting (HTS) motor for aircraft propulsion was designed and analyzed [15]. Magnetic forces and stiffness for an axial flux machine using passive magnetic bearing with axial magnetization were analyzed on wind and hydro low-speed turbines [16]. The modeling of the axial magnetic force and stiffness of a ring-shaped PM passive vibration isolator was presented [17]. The modeling of electromagnetic (EM) force and axial-stiffness for an EM negative-stiffness spring toward vibration isolation was presented [18]. The magnetic forces and axial-stiffness were analyzed for a new axial-type superconducting magnetic bearing (SMB) based on the interaction behavior between a PM and two closed superconducting coils [19].

A comparison of the axial stiffness of journal bearings in FC and ZFC cooling modes was made [20]. This paper aims to evaluate ways to passively augment the axial stiffness of studied horizontal axis HTS ZFC radial levitation bearing so that it may compete in terms of guiding stability with FC superconducting bearings. Section 2 focuses on presenting designs and materials for the existing and modified bearing geometries and describing the adopted analysis methods to reduce numerical processing. Section 3 presents result on determining and validating the equivalent magnetic permeability when the rotor and stator axes are aligned. Also, on the evaluation of the axial stiffness augmentation with the addition of HTS bulks in the stator or limiting PM rings aligned with the rotor. Results are discussed in Section 4 and the main conclusions stated in Section 5.

2. Materials and Methods

This section presents and describes the designs, materials, and analysis methods considered in the studies.

2.1. Designs and Materials

The considered HTS ZFC horizontal axis radial levitation Passive Magnetic Bearing (PMB) topology includes a stator housing two discontinuous rings, each one with up to eight High-Temperature Superconductor (HTS) bulks, and a Permanent Magnet (PM) rotor with three radially magnetized continuous PM rings, the polarization of the intermediate one opposite from the side PM rings. Each discontinuous ring of HTS bulks in the zone between the middle PM ring and one side PM ring. HTS bulks of Yttrium Barium Copper Oxide (YBCO) and PM rings of Neodymium Iron Borum (NdFeB) with grade N40 have been used in experimental prototypes and considered for 3D Finite Element Analysis (FEA).

Guiding optimization studies were performed [12] considering both bulks of dimensions $33 \times 33 \times 14\ \mathrm{mm}^3$ and $40 \times 40 \times 10\ \mathrm{mm}^3$. The results have shown that besides the first ones generate guidance forces slightly higher, with the second ones the magnetic levitation is higher. For this reason and because of the availability of good condition bulks of dimensions $40 \times 40 \times 10\ \mathrm{mm}^3$ in our laboratory, only this bulk size is considered in the studies presented in this document. Figures 2(a) and 2(b) show the dimensioned longitudinal bisection design of the studied bearing topology and corresponding mesh grid for 3D FEA. Variables d_{sc} and d_m refer to the distances respectively between the two discontinuous rings of HTS bulks in the stator and between adjacent PM rings in the rotor.

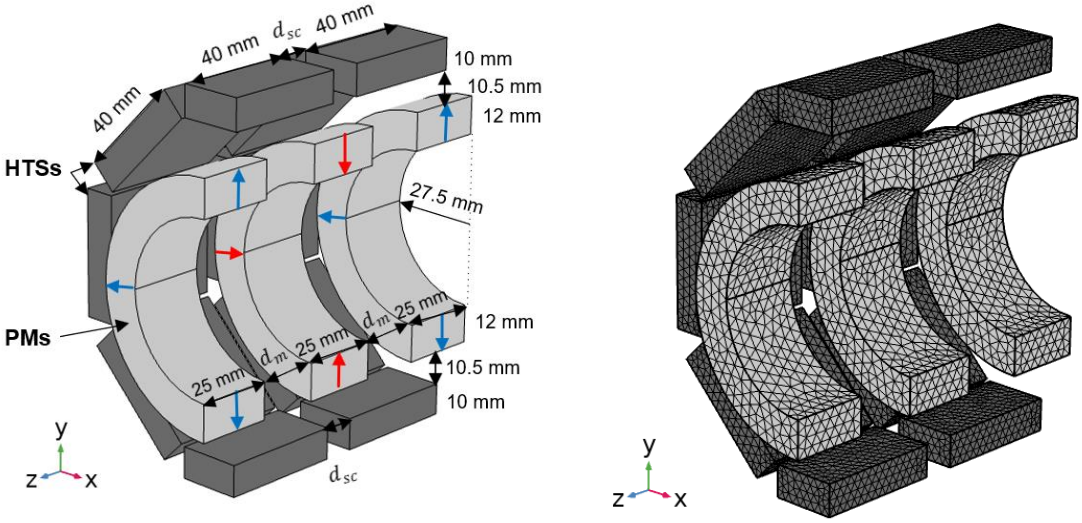

(**a**) (**b**)

Figure 2. Dimensioned design of a longitudinal bisection of the studied radial levitation bearing (a) and corresponding mesh grid considered for 3D FEA (b).

To facilitate the process of ZFC, after the ZFC of HTS bulks, the rotor was always placed in the stator cavity with the rotor and stator axes aligned. Thus, by completing the stator with a total of sixteen HTS bulks, referred as to Topology A, it would be impossible to levitate with the rotor axis at the center position. With this topology of HTS bulks, distributed symmetrically in the stator, the resulting magnetic levitation force in the y direction would be zero, and gravity pulls the rotor down forcing it to levitate with eccentricity.

Figures 3(a) to 3(f) show different possible topologies of asymmetric distribution of HTS bulks in the stator. Figures 3(e) and 3(f) show respectively Topology F with a negative vertical deviation of the rotor ($\Delta y < 0$) and Topology G with a positive vertical deviation of the rotor ($\Delta y > 0$). The dashed lines refer to the rotor position at $\Delta y = 0$, with the rotor and stator axes aligned.

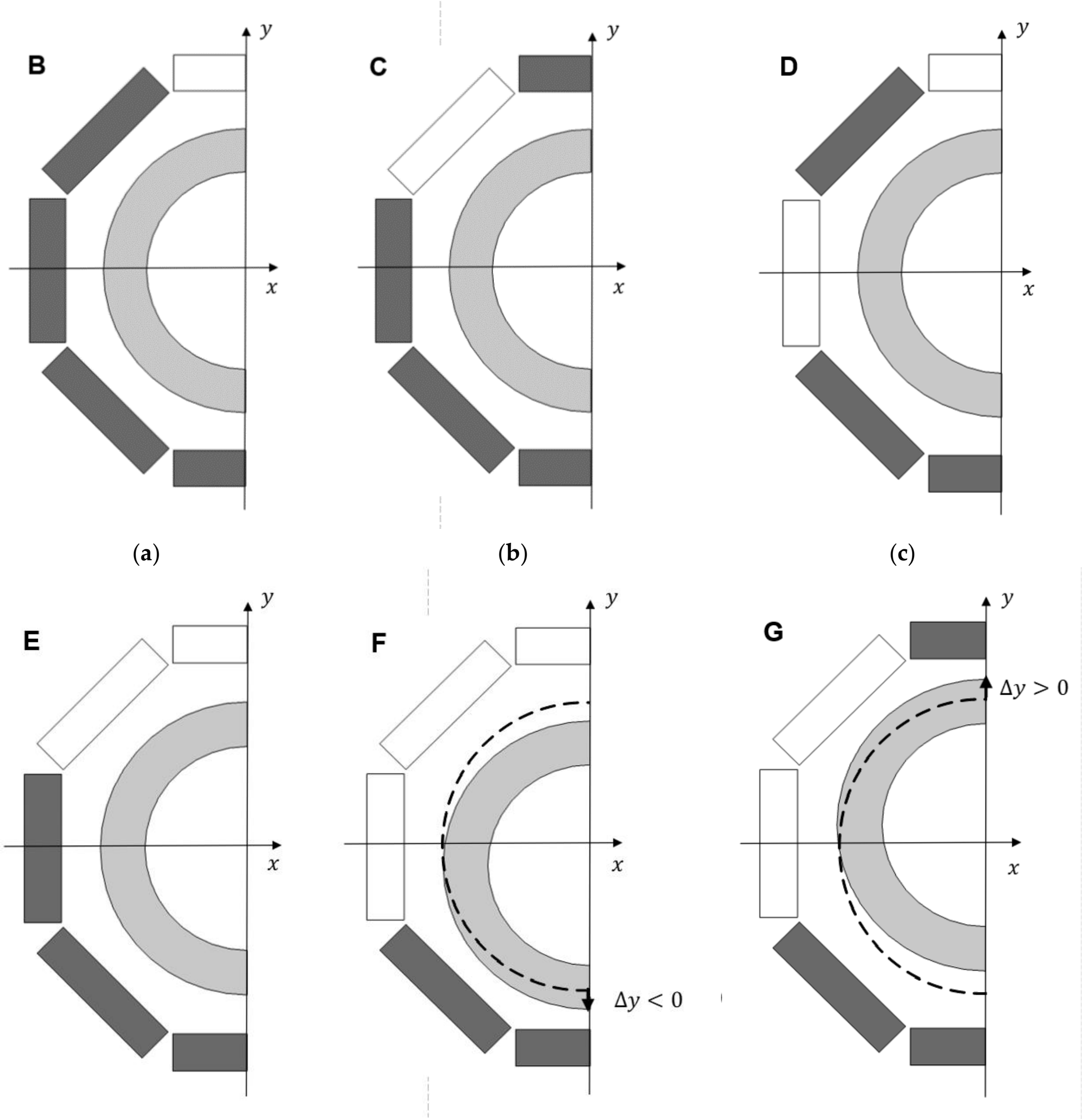

(a) (b) (c)

(d) (e) (f)

Figure 3. Lateral views of the longitudinal bisection design for six different topologies with asymmetric distribution of HTS bulks in the stator, namely topology B (a), topology C (b), topology D (c), topology E (d), topology F (e), and topology G (b).

Topology F with only six HTS bulks at the stator bottom, maximizes the resulting magnetic force in the y direction, referred to as levitation force, with less investment on HTS bulks. Because this topology enables a wider range of vertical deviations Δy where levitation is verified, it was considered in previous studies for the validation by experimental testing of magnetic forces predicted by numerical FEA. On the other hand, the verified magnetic guidance forces are minimal with Topology F, because the higher the magnetic energy portion used for levitation, the lower the magnetic energy portion used for guidance.

Figures 4(a) and 4(b) show views of longitudinal bisections respectively for Topology F with a negative axial deviation of the rotor ($\Delta z < 0$) and for Topology G with a positive axial deviation of the rotor ($\Delta z > 0$). The dashed lines refer to the rotor position at $\Delta z = 0$.

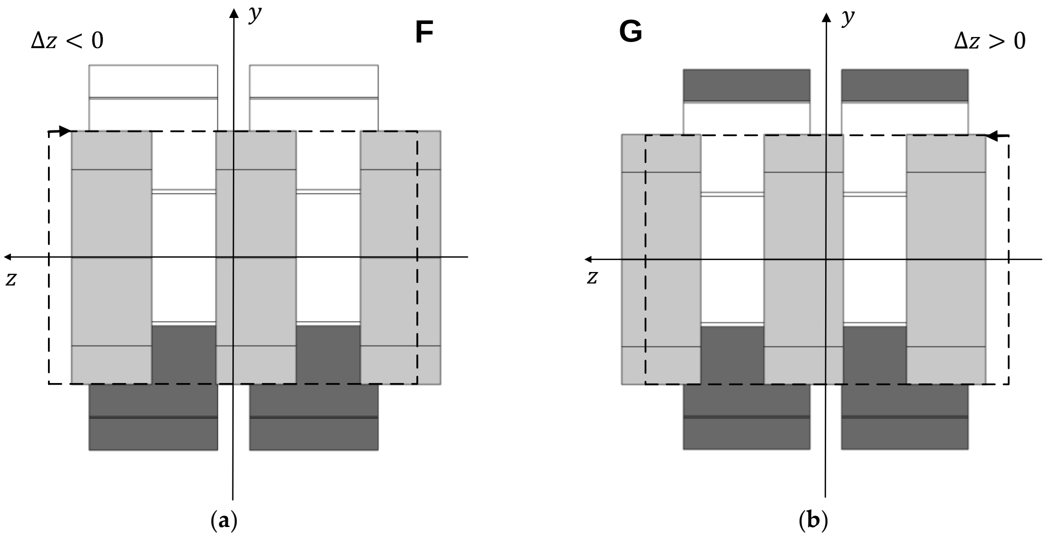

(**a**) (**b**)

Figure 4. Views of longitudinal bisections respectively for Topology F with a negative axial deviation of the rotor ($\Delta z < 0$) in (a) and for Topology G with a positive axial deviation of the rotor ($\Delta z > 0$) in (b).

Figure 5 shows the design of the proposed change in adding two limiting radially magnetized PM rings with the same polarization as the rotor edge PM rings, to significantly increase the axial stiffness with no significant additional investment. Variable d_{ml} represents the distance between the rotor edge PM rings and the limiting PM rings, with no axial deviation of the rotor ($\Delta_z = 0$).

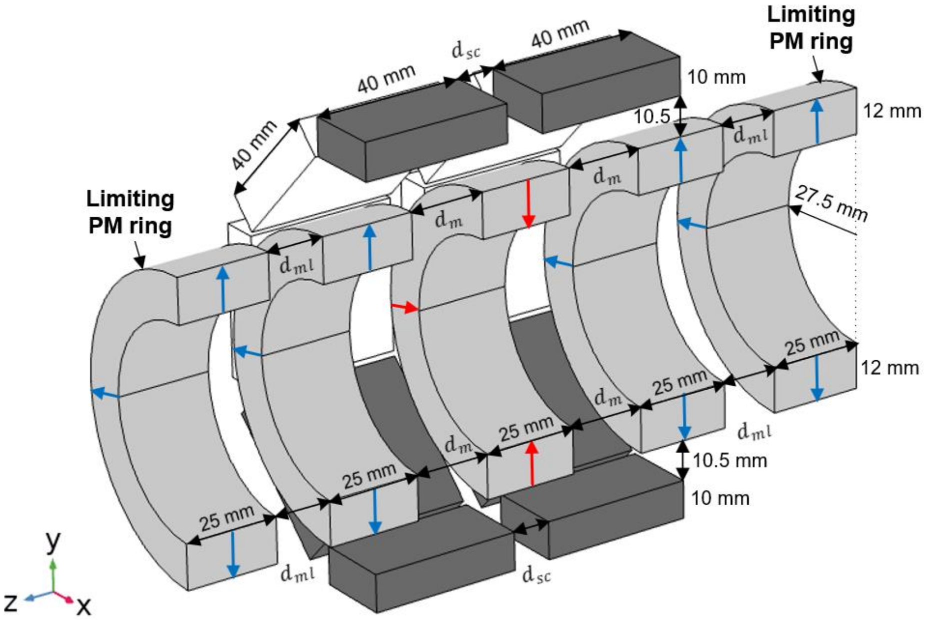

Figure 5. Design of the proposed change, adding two limiting radially magnetized PM rings with the same polarization as the rotor edge PM rings to significantly increase the axial stiffness.

2.2. *Adopted Method to Reduce Numerical Processing in the Prediction of Magnetic Guidance Forces*

The required numerical processing in 3D FEA prediction of magnetic forces could be significantly reduced if a simplified model of equivalent permeability is considered for HTS bulks [11, 21]. This approach avoids performing a complete electromagnetic analysis using non-linear conductivity power laws and the Kim-Anderson model for type II superconductors to determine the detailed current distributions and magnetization of HTS bulks. [22, 23], while providing accurate results if an appropriate magnetic permeability is considered.

Previous results [11, 12] have shown that for the considered ZFC radial bearing, the equivalent permeability of HTS bulks varies with the rotor vertical deviation. Their equivalent permeability does not notably vary on the limited range of possible rotor axial deviations when kept with no radial deviation. Once the prediction and validation of magnetic guidance forces are performed keeping the rotor and stator axes coincident (with no radial deviation of the rotor), the FEA numerical prediction of magnetic guidance forces is determined assuming the approximate value of equivalent magnetic permeability for the HTS bulks verified when there is no rotor radial deviation. Results related to the determination and validation of such equivalent magnetic permeability values are presented in subsection 3.1.

3. Results

This section first presents results of determining and validating the HTS bulks' equivalent magnetic permeability with no rotor radial deviation. Then, results on the axial stiffness depending on the considered topology and number of HTS bulks in the stator are presented. At the end, results concerning the determination and validation of the axial stiffness augmentation by adding limiting PM rings with the same polarization as the rotor edge PM rings, are presented.

3.1. Equivalent Magnetic Permeability for HTS Bulks with no Radial Deviation of the PM Rotor

The validation of the HTS bulks' equivalent permeability with no radial deviation of the PM rotor was performed considering Topology F because this topology maximizes the range of rotor vertical deviations where levitation is verified. Also, with this topology, the number of HTS bulks is only six, minimizing the required numerical processing. The six HTS bulks are located on the lower half of the stator, being enough to determine and validate the variation of the HTS bulks' magnetic permeability with the rotor vertical deviation considering that the bearing geometry presents symmetry with relation to the horizontal plane of longitudinal bisection.

Figure 6(a) shows the distribution of magnetic field density **B** resultant from 3D FEA simulations with no radial deviation of the PM rotor considering HTS bulks with equivalent magnetic permeability $\overline{\mu_r} = 0.25$. Figure 6(b) shows the distributions of **B** and detailed current density **J** obtained considering the complete electromagnetic non-linear power-law model for the conductivity of type II superconductors with $J_{c0} = 5 \times 10^{-7}$ Am^{-2}. The obtained distribution of **B** nearby HTS bulk boundaries is similar with the two models.

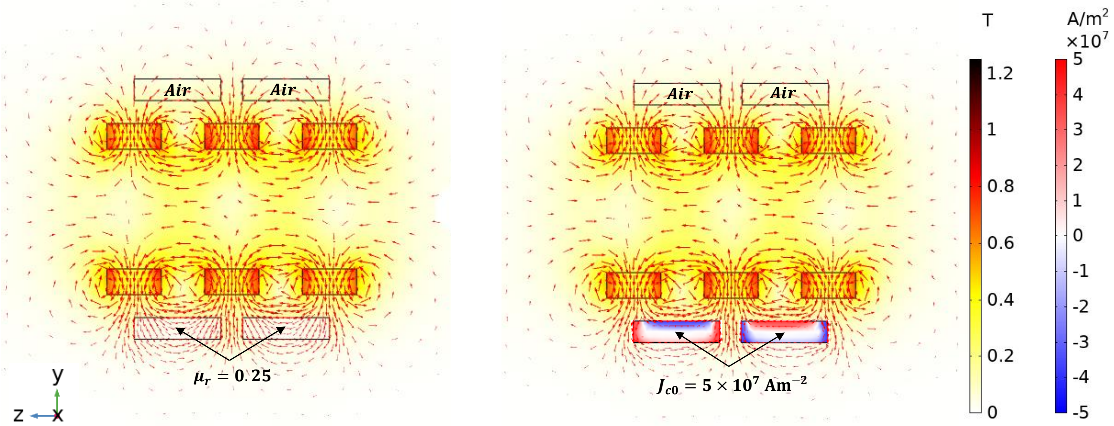

(**a**) (**b**)

Figure 6. Distributions obtained by 3D FEA simulations for **B** considering HTS bulks with $\mu_r = 0.25$ (a), and for **B** and **J** considering the complete EM model with $J_{c0} = 5 \times 10^{-7}$ Am^{-2} (b).

Figure 7(a) shows the experimental measurement of the magnetic levitation force $\mathbf{F}_{\mathbf{lev}}$ with no vertical deviation ($\Delta y = 0$) and no axial deviation ($\Delta z = 0$) of rotor D20 ($d_m = 20$ mm). The measured levitation force magnitude $\mathrm{F}_{\mathrm{lev}} = 27.01$ N, is the sum of the rotor gravity $\mathrm{F}_{\mathrm{g}} = 15.88$ N with the impulsion force measured with Baxtran KRN05 dynamometer $\mathrm{F}_{\mathrm{m}} = 11.13$ N. Figure 7(b) shows the experimental measurement of the magnetic guidance force $\mathbf{F}_{\mathbf{gui}}$ with no vertical deviation $(\Delta y = 0)$ and an axial deviation $\Delta z = -10$ mm of rotor D20 where the predicted guidance force is maximum. The measured guidance force with $\Delta y = 0$ and $\Delta z = -10$ mm was $\mathrm{F}_{\mathrm{gui}} = +4.55$ N.

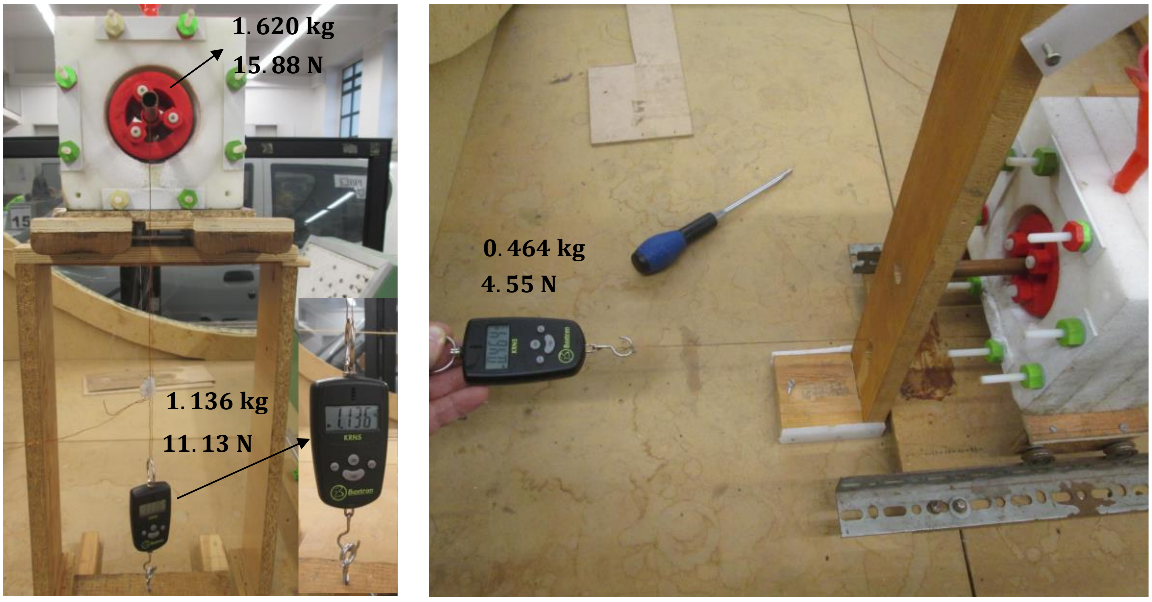

(**a**) (**b**)

Figure 7. Experimental measurement of $\mathbf{F}_{\mathbf{lev}}$ with Topology F and rotor D20 at $\Delta y = 0$ and $\Delta z = 0$ (a), and of $\mathbf{F}_{\mathbf{gui}}$ with Topology F and rotor D20 at $\Delta y = 0$ and $\Delta z = -10$ mm (b).

Figure 8 shows the characteristics $\mathrm{F}_{\mathrm{lev}}(\Delta y)$ with $\Delta z = 0$, predicted by 3D FEA simulations. Five were obtained considering equivalent values of μ_r ranging from 0.2 to 0.4, and one (red line) obtained using the complete electromagnetic model with $J_{c0} = 5 \times 10^{-7}\ \mathrm{Am}^{-2}$.

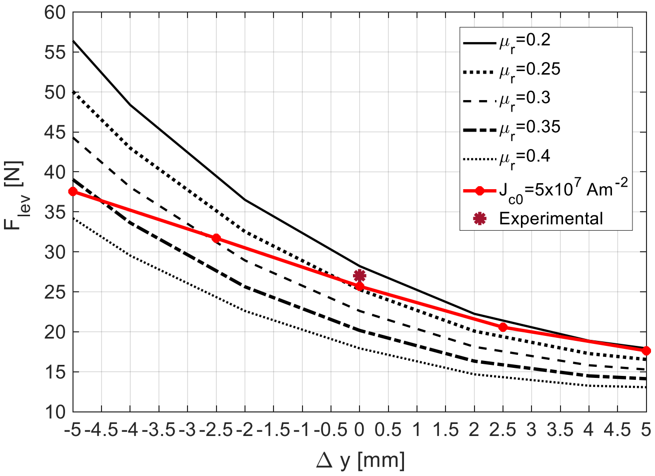

Figure 8. Characteristics $\mathrm{F}_{\mathrm{lev}}(\Delta y)$ with $\Delta z = 0$, using Topology F and rotor D20, predicted by 3D FEA for $\overline{\mu_r}$ ranging from 0.2 to 0.4 and for $J_{c0} = 5 \times 10^{-7}\ \mathrm{Am}^{-2}$.

According to [11, 12] the characteristic $\mathrm{F}_{\mathrm{lev}}(\Delta y)$ with $\Delta z = 0$, resultant from experimental measurements using rotor D20 ($\mathrm{d}_{\mathrm{m}} = 20$ mm), follows in between the two ones predicted by 3D FEA simulations using the complete electromagnetic model with $J_{c0} = 3 \times 10^{-7}\ \mathrm{Am}^{-2}$ and $J_{c0} = 8 \times 10^{-7}\ \mathrm{Am}^{-2}$. The characteristic obtained considering $\overline{\mu_r} = 0.25$ crosses the one obtained with the complete model considering $J_{c0} = 5 \times 10^{-7}\ \mathrm{Am}^{-2}$, at almost $\Delta y = 0$ (no vertical deviation of the rotor). Also, the experimental measurement of the levitation force at $\Delta y = 0$ $(\mathrm{F}_{\mathrm{lev}} = 27.01\ \mathrm{N})$ is close to the predicted one at the point close to $\Delta y = 0$ where the two characteristics for $\overline{\mu_r} = 0.25$ and $J_{c0} = 5 \times 10^{-7}$ Am^{-2} cross each other.

Figure 9 shows the characteristics $\mathrm{F}_{\mathrm{gui}}(\Delta z)$ with $\Delta y = 0$, predicted by 3D FEA simulations. Five were obtained considering equivalent values of $\overline{\mu_r}$ ranging from 0.2 to 0.4, and one (red line) obtained using the complete electromagnetic model with $J_{c0} = 5 \times 10^{-7}$ Am^{-2}. The experimental measurement of the guidance force at $\Delta z = -10$ mm ($\mathrm{F}_{\mathrm{gui}} = +4.55$ N) is close to the predicted ones considering $\overline{\mu_r} = 0.25$ and $J_{c0} = 5 \times 10^{-7}$ Am^{-2}.

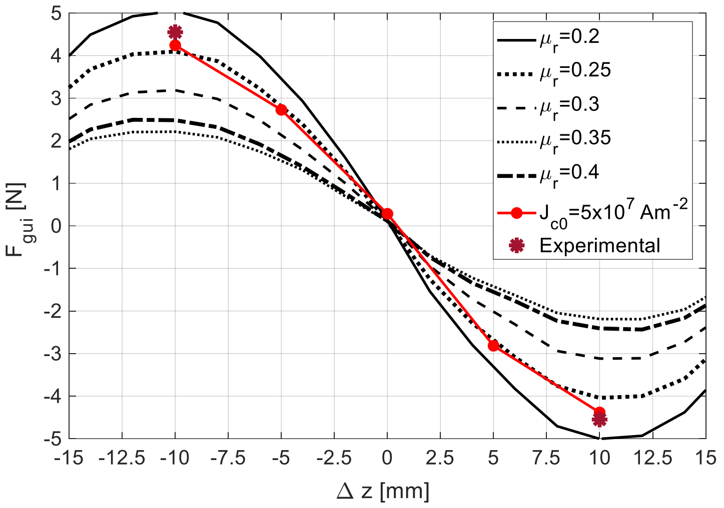

Figure 9. Characteristics $\mathrm{F}_{\mathrm{gui}}(\Delta z)$ with $\Delta y = 0$, using Topology F and rotor D20, predicted by 3D FEA for μ_r ranging from 0.2 to 0.4 and for $J_{c0} = 5 \times 10^{-7}$ Am^{-2}.

From the obtained results one may conclude that keeping the rotor and stator axes coincident (no rotor vertical deviation $\Delta y = 0$), the verified equivalent magnetic permeability remains almost constant for values of axial deviation Δz ranging from 0 to ± 10 mm, assuming a value close to $\overline{\mu_r} = 0.25$.

3.2. Axial Stiffness Augmentation by Adding HTS Bulks to the Stator

Figure 10 shows the dependence of $\mathrm{F}_{\mathrm{lev}}$ with the distance d_m between adjacent PM rings in the rotor, obtained by 3D FEA considering the HTS bulks with an equivalent magnetic permeability $\overline{\mu_r} = 0.25$, for the several topologies of HTS bulks in the stator. This is done, keeping the rotor at the axial equilibrium position ($\Delta z = 0$) with its axis coinciding with the stator axis ($\Delta y = 0$).

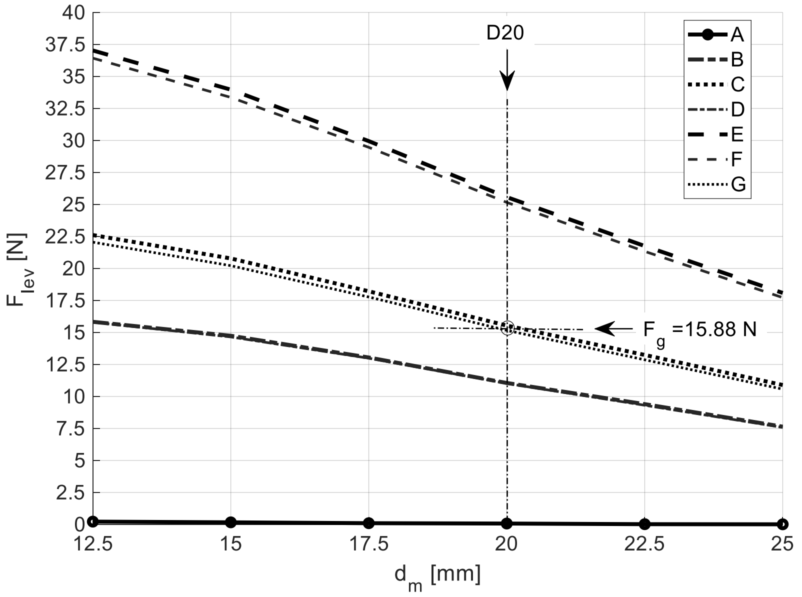

Figure 10. Dependence of $\mathrm{F}_{\mathrm{lev}}$ with d_m keeping the rotor at $\Delta y = 0$ and $\Delta z = 0$, for the several topologies of HTS in the stator, considering $\overline{\mu_r} = 0.25$.

The levitation force $\mathrm{F}_{\mathrm{lev}}$ decreases with the increase of the distance d_m between adjacent PM rings in the rotor. The generated levitation assumes higher values with topologies E and F. The values of $\mathrm{F}_{\mathrm{lev}}$ for these two topologies are close because the HTS Bulks with higher surfaces disposed vertically in Topology E almost do not contribute to levitation. The investment with Topology E including ten HTS bulks is higher than with topology F including six HTS bulks, but Topology E guarantees higher stiffness in the x direction. A similar thinking could be done by comparing topologies C and G. Thus, the investment with Topology C is higher than with Topology G, but Topology C guarantees higher stiffness in the x direction. With topologies C and G, it is possible to keep rotor D20 ($d_m = 20$ mm) levitating with a vertical deviation close to $\Delta y = 0$, because its gravity force is $\mathrm{F}_{\mathrm{g}} = 15.88$ N.

Figures 11(a) and 11(b) show respectively for rotors with $d_m = 20$ mm and $d_m = 15$ mm, the dependence of the guidance $\mathrm{F}_{\mathrm{gui}}$ with the rotor axial deviation Δz keeping its axis coinciding with the stator axis ($\Delta y = 0$), obtained by 3D FEA considering an equivalent relative magnetic permeability $\overline{\mu_r} = 0.25$. This dependence was predicted for the several topologies of HTS bulks in the stator.

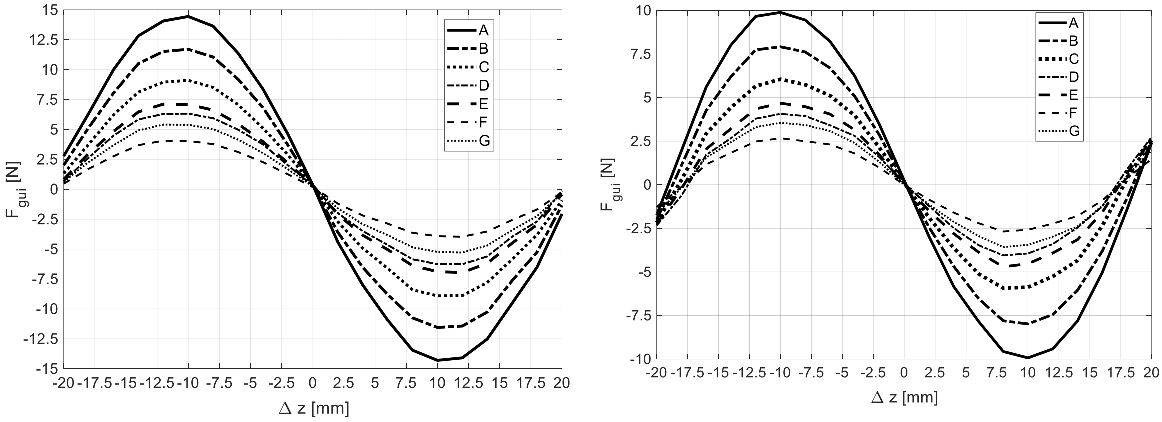

(**a**) (**b**)

Figure 11. Dependence of $\mathrm{F}_{\mathrm{gui}}$ with Δz, keeping rotors defined by $d_m = 20$ mm (a) and $d_m = 15$ mm (b) at $\Delta y = 0$, for the several topologies of HTS in the stator, predicted by 3D FEA considering $\overline{\mu_r} = 0.25$.

The guidance force $\mathrm{F}_{\mathrm{gui}}$ is higher with $d_m = 20$ mm than with $d_m = 15$ mm. This force depends on the number of HTS bulks in the stator, increasing with the number of HTS bulks of the considered topology. Table 1 states the axial stiffness κ with rotor D20 ($d_m = 20$ mm) within $\Delta z = \pm 5$ mm, for several topologies of HTS bulks in the stator that allow the rotor levitation with positive vertical deviation ($\Delta y \geq 0$) according to Figure 10.

Table 1. Axial stiffness with rotor D20 ($d_m = 20$ mm) within $\Delta z = \pm 5$ mm, for several topologies of HTS bulks, that allow the levitation of such rotor with $\Delta y \geq 0$.

Topology	**# HTS bulks**	**κ [N mm^{-1}]**
F	6	0.31
G	8	0.58
E	10	0.94
C	12	1.21

Topology F was considered in previous studies for the reasons explained in subsections 2.1 and 3.1. When moving from Topology F to topologies G, E, or G there will be a significant investment in the number of additional HTS bulks needed. The axial stiffness with Topology C is still low, making the studied horizontal axis HTS ZFC radial levitation PMB inappropriate for applications requiring high-precision axial stability.

3.3. Axial Stiffness Augmentation by Adding Limiting PM Rings

The axial stiffness does not increase significantly when HTS bulks are added to the stator. The addition of two limiting PM rings radially magnetized with the same polarization as the rotor edge PM rings to significantly increase the axial stiffness of the studied PMB is evaluated here.

Figure 12 shows the experimental setup to measure the magnetic impulsion force F_{ml} between the limiting PM ring on one side and the closest rotor edge PM ring depending on distance d_{ml}. Figure 13 shows measurements of F_{ml} for distances d_{ml} equal to: a) 5 mm, b) 10 mm, c) 15 mm, and d) 20 mm.

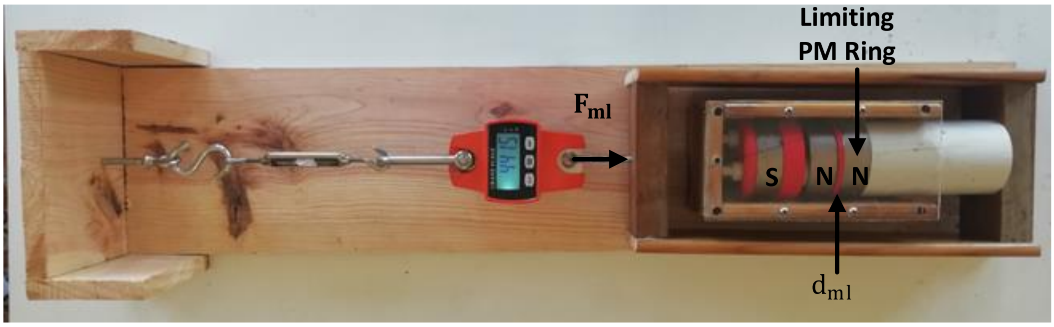

Figure 12. Experimental setup to measure the magnetic impulsion force F_{ml} between the limiting PM ring on one side and the closest rotor edge PM ring, depending on distance d_{ml}.

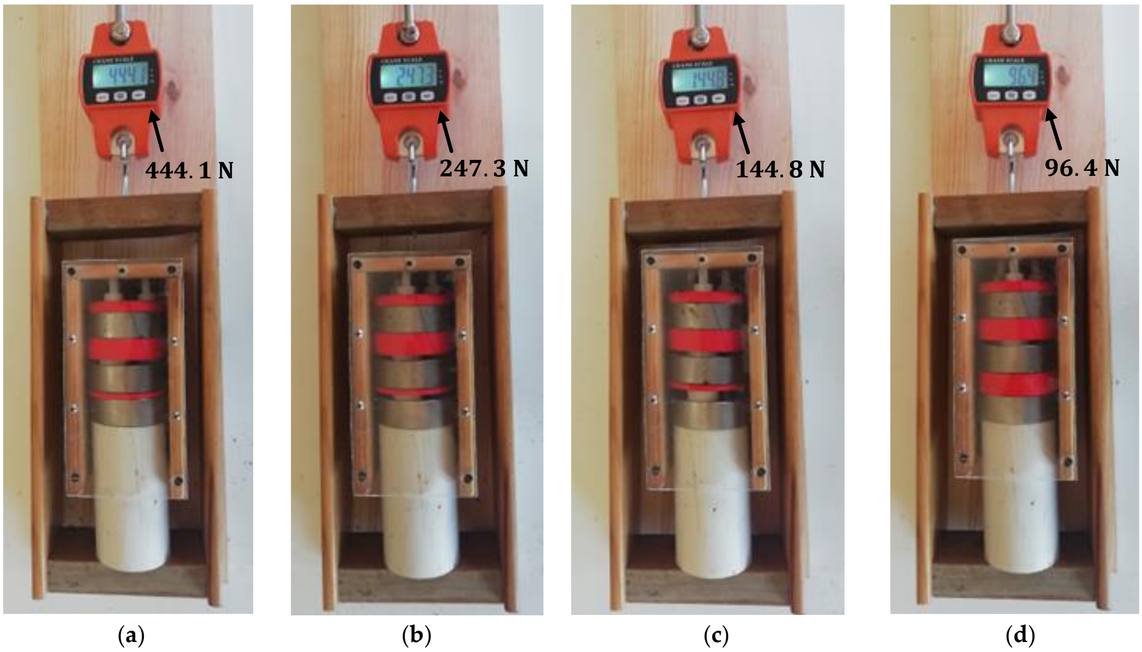

Figure 13. Measurements of F_{ml} for distances d_{ml} equal to 5 mm (a), 10 mm (b), 15 mm (c), and 20 mm (d).

Figure 14 shows the characteristics of the magnetic impulsion force F_{ml} between the limiting PM ring on one side and the closest rotor edge PM ring depending on distance d_{ml}, predicted by 3D FEA and obtained experimentally. The experimental measurements follow with good approximation the characteristic predicted by 3D FEA.

The total guidance force $\mathbf{F_{gui}}^{+}$ of the modified horizontal axis HTS ZFC passive bearing including limiting PMs results from the sum of the basic bearing guidance force $\mathbf{F_{gui}}$ with the additional guidance force $\mathbf{F_{gui}}'$ from the limiting PM rings impulsion action, as expressed by equation (1):

$$\mathbf{F_{gui}}^{+} = \mathbf{F_{gui}} + \mathbf{F_{gui}}' \qquad (1)$$

Dividing both members of equation (1) by Δz results that the total guiding stiffness κ^{+} of the modified horizontal axis HTS ZFC passive bearing including limiting PMs results from the sum of the basic bearing guiding stiffness κ with the additional guiding stiffness κ' from limiting PMs impulsion action. This can be modelled by a spring that results from the parallel of two springs.

$$\kappa^{+} = \frac{F_{gui}{}^{+}}{\Delta z} = \frac{F_{gui} + F_{gui}{}'}{\Delta z} = \frac{F_{gui}}{\Delta z} + \frac{F_{gui}{}'}{\Delta z} = \kappa + \kappa\,' \quad (2)$$

Figure 15 shows the characteristics of the total guidance force $F_{gui}{}^{+}$ as a function of the axial deviation Δz for distances d_{ml} equal to 5 mm, 10 mm, 15 mm, and 20 mm. These characteristics were predicted by 3D FEA considering the use of rotor D20 ($d_m = 20$ mm) and the HTS bulks with an equivalent relative permeability $\overline{\mu_r} = 0.25$ distributed in the stator according to Topology G.

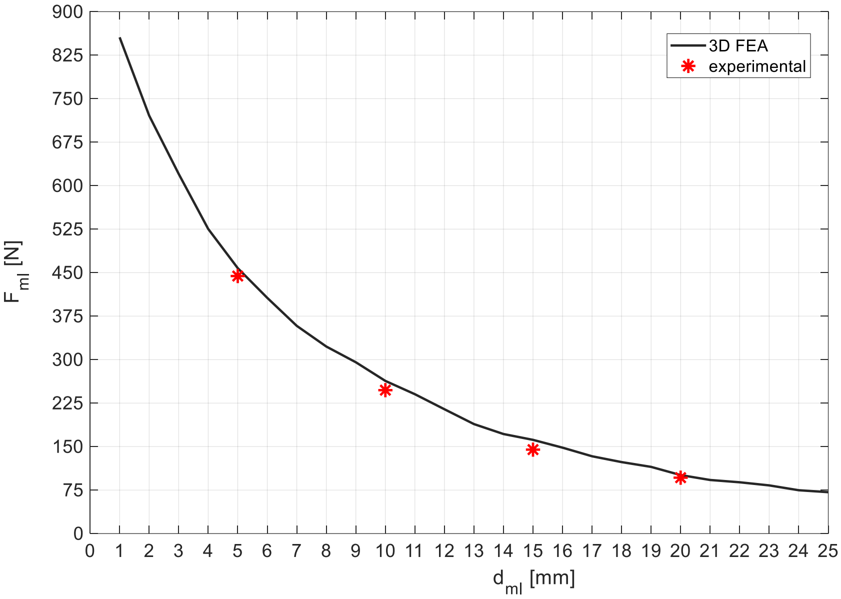

Figure 14. Characteristics of the magnetic impulsion force F_{ml} between the limiting PM ring on one side and the closest rotor edge PM ring as a function of the distance d_{ml} in between them, predicted by 3D FEA and obtained experimentally.

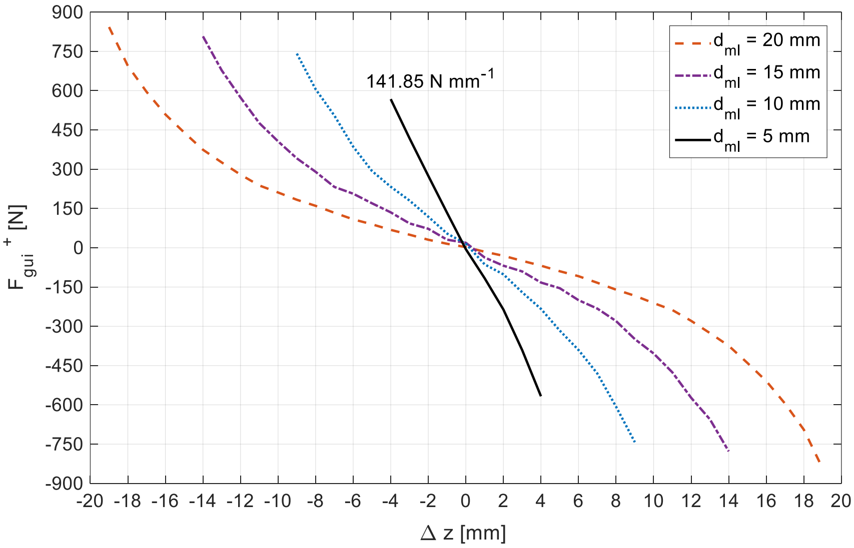

Figure 15. Characteristics of the total guidance force ${F_{gui}}^{+}$ as a function of the axial deviation Δz, considering the use of rotor D20 ($d_m = 20\,\mathrm{mm}$) and the HTS bulks with an equivalent relative permeability $\overline{\mu_r} = 0.25$ distributed in the stator according to Topology G.

With limiting PM rings placed at a distance $d_{ml} = 5\,\mathrm{mm}$ from the rotor edge PM rings, limiting the rotor axial deviation to $\Delta z = \pm 5\,\mathrm{mm}$, the total predicted axial stiffness would be $\kappa^{+} = 141.85\,\mathrm{N\,mm^{-1}}$. This value is significantly higher (more than one hundred times) than the one presented in Table 1 for topology G without limiting PM rings.

4. Discussion

With addition of HTS bulks in the stator, magnetic guidance forces increase but on the other hand magnetic levitation forces decrease. Topology F with only six HTS bulks at the bottom of the stator, is the one that guarantees higher levitation but on the other hand is the more unstable topology. Because Topology F enables a wider range of vertical deviations for testing, this topology was used on the prediction and evaluation of the HTS bulks' equivalent relative permeability as a function of the rotor vertical deviation.

According to Figure 10, with topologies C, E, F, and G of HTS bulks in the stator, the PM rotor D20 can levitate at vertical deviations $\Delta y \geq 0$. When moving from Topology F to Topology E, the levitation remains the same, but the guidance force increases about 95%. Topologies C and G provide almost equal levitation forces, that are about 61% of the levitation with topologies E and F. The guidance force with topologies C and G are about respectively 143% and 42% higher than with Topology F. So, when moving from Topology F to Topology G, with only two more HTS bulks, the levitation is reduced to 61% and the guidance increased about 42% than with topology F. When moving from Topology F to Topology C, six additional bulks are needed, representing a significative investment, to get a guidance increase that is insufficient for applications requiring high-precision axial stability.

With the passive addition of two limiting PM rings, the axial stiffness increases significantly (more than one hundred times) considering a distance d_{ml} between limiting PM rings and rotor side PM rings equal to 5 mm. This enables the use of the modified HTS ZFC bearing for applications of high-precision axial stability.

5. Conclusions

The base geometry of the horizontal axis HTS ZFC radial passive magnetic bearing generates guiding stability when the distance between side the rotor side PM rings is higher than the distance between the edges of discontinuous HTS bulk rings in the stator [12]. The values of generated guidance forces by the basic geometry do not permit its application for high-precision axial stability applications such as precision gyroscopes, horizontal axis propellers and turbines. The results presented in this study have shown that with the addition of HTS bulks in the stator, that is traduced by a relevant cost increase, the guidance forces do not increase significantly remaining of the same order and still cannot be used for high-precision axial stability applications.

A modification is proposed consisting of the addition of two limiting PM rings, placed at a fixed distance from the rotor edges considering no rotor axial deviation and with the same polarization as the rotor side PM rings. Results show that for the distance d_{ml} between limiting PM rings and rotor side PM rings equal to $5\ \mathrm{mm}$, the obtained total axial stiffness is $\kappa^{+} = 141.85\ \mathrm{N\ mm^{-1}}$ which is more than one hundred times higher than the axial stiffness for the base geometry κ. With such modification, the HTS ZFC radial passive bearing may be used on applications of high-precision axial stability.

Author Contributions: Conceptualization, A.J.A.C., and P.J.C.B.; methodology, A.J.A.C., and J.F.P.F; software, A.J.A.C., and J.F.P.F; validation, A.J.A.C., J.F.P.F, and P.J.C.B.; formal analysis, J.F.P.F, and P.J.C.B.; investigation, A.J.A.C.; resources, P.J.C.B.; data curation, A.J.A.C., and J.F.P.F; writing—original draft preparation, A.J.A.C.; writing—review and editing, A.J.A.C., J.F.P.F, and P.J.C.B.; supervision, J.F.P.F, and P.J.C.B.; project administration, J.F.P.F, and P.J.C.B.; funding acquisition, J.F.P.F, and P.J.C.B. All authors have read and agreed to the published version of the manuscript.

Funding: This research was funded by *Fundação para a Ciência e a Tecnologia* (FCT) for its financial support via the project LAETA Base Funding (DOI: 10.54499/UIDB/50022/2020).

Data Availability Statement: The data presented in this study are available on request from the corresponding author. The data are not publicly available due to privacy.

Conflicts of Interest: The authors declare no conflicts of interest.

References

1. Li, S.L.; Wen, H.H.; Zhao, Z.X. Modeling and simulation on the magnetization in field-cooling and zero-field-cooling processes. *Physica C: Superconductivity*, **1999**, *316(3-4)*, pp. 293-299.
2. Yang, W.M.; Zhou, L.; Feng, Y.; Zhang, P. X.; Nicolsky, R.; de Andrade, R. The characterization of levitation force and attractive force of single-domain YBCO bulk under different field cooling process. *Physica C: Superconductivity*, **2003**, *398(3-4)*, pp. 141–146.
3. Fujishiro, H.; Naito T. Simulation of temperature and magnetic field distribution in superconducting bulk during pulsed field magnetization. *Superconductor Science and Technology*, **2010**, 23, 105021, pp. 1-8.
4. Arnaud, J.; Branco P.J.C. Electrothermal characteristics of YBCO bulk magnets deep in LN2: a preliminary analysis for its use as excitation system of low-speed synchronous generators. *IEEE Transactions on Applied Superconductivity*, **2016**, *26(3)*, pp. 1-8.
5. Ceniga, L.; Diko, P. Matrix crack formation in Y–Ba–Cu–O superconductor. *Phys. C*, **2003**, 385, pp. 329–336.
6. Diko, P.; Krabbes, G. Formation of c-macrocracks during oxygenation of TSMG YBa2Cu3O7/Y2BaCuO5 single-grain superconductors. *Phys. C*, **2003**, 399, pp. 151–157.
7. Arsénio, A.J.; Roque, M.; Cardeira, C.; Branco, P.J.C.; Melicio, R. Prototype of a Zero-Field-Cooled YBCO Bearing with Continuous Ring Permanent Magnets. *IEEE Trans. Appl. Superconductivity*. **2018**, *28(4)*, pp. 1–7.
8. Arsénio, A.J.; Melicio, R.; Cardeira, C.; Costa Branco, P.J. The Critic Liquid-gas Phase Transition between Liquid Nitrogen and YBCO HTS bulks: from FEM Modeling to Its Experimental Study for ZFC Levitation Devices. *IEEE Transactions on Applied Superconductivity*, **2018**, *28(4)*, pp. 1-6.
9. Arsénio Costa, A.J.; Fernandes, J.F.P.; Melicio, R.; Cardeira, C.; Costa Branco P.J. Numerical and Experimental Analysis of the ZFC Heat Release from a YBCO Bulk and Validation of YBCO Thermal Parameters. *MDPI, Crystals*, **2023**, *13(3)*, 532, pp. 1–16.
10. Costa Arsénio, A.J.; Costa Branco, P.J. Thermo-Hydraulic Analysis of a Horizontal HTS ZFC Levitating Bearing Concerning Its Autonomy Safety Service Time. *IEEE Transactions on Applied Superconductivity*, **2021**, *31(5)*, pp. 1–10.
11. Fernandes, J.F.P.; Arsénio Costa, A.J.; Arnaud J. Optimization of a Horizontal Axis HTS ZFC Levitation Bearing using Genetic Decision Algorithms over Finite Element Results. *IEEE Transactions on Applied Superconductivity*, **2020**, *30(2)*, pp. 1–20.
12. Arsénio, A.J.; Silva, F.F.; Fernandes, J.F.P.; Branco, P.J.C. Optimization of the Guiding Stability of a Horizontal Axis HTS ZFC Radial Levitation Bearing. *MDPI, Actuators*, **2021**, 10(12), 311, pp. 1–21.

13. Sun, J.; Chen, D.; Ren, Y. Stiffness Measurement Method of Repulsive Passive Magnetic Bearing in SGMSCMG. IEEE *Transactions on Instrumentation and Measurement*, **2013**, 62(11), pp. 1–10.
14. McDonald, A.; Jaen-Sola, P. A Stiffness Approach for Coupling Structural and Magnetic Models for the Sustainable Design, Optimisation and Real-Time Structural Integrity Assessment of Radial Flux Permanent Magnet Generators for Direct-Drive Wind Turbines. *MDPI, Sustainability,* **2024**, *16*(6), 2393, pp. 1–21.
15. AlizadehTir, M.; Marignetti, F.; Mirimani S.M. Axial Flux Machine Using Passive Magnetic Bearing With Axial Magnetization. *IEEE International Symposium on Power Electronics, Electrical Drives, Automation and Motion*, **2018**, pp. 1–6.
16. Lee, J.-Y.; Nam, G.-D.; Yu, I.-K.; Park, M. Design and Characteristic Analysis of an Axial Flux High-Temperature Superconducting Motor for Aircraft Propulsion. *MDPI, Materials*, **2023**, 16, 3587, pp. 1–13.
17. Zhu, Y.; Li, Q.; Xu, D.; Zhang, M. Modeling of Axial Magnetic Force and Stiffness of Ring-Shaped Permanent-Magnet Passive Vibration Isolator and Its Vibration Isolating Experiment. *IEEE Transactions on Magnetics*, **2012**, *48(7)*, pp. 1–11.
18. Sun, Y.; Meng, K.; Yuan, S.; Zhao J.; Xie R.; Yang, Y.; Luo J. Modeling Electromagnetic Force and Axial-Stiffness for an Electromagnetic Negative-Stiffness Spring Toward Vibration Isolation. *IEEE Transactions on Magnetics*, **2019**, *55(3)*, pp. 1–10.
19. Li, W.; Yang, T.; Xin, Y. Principle, Modeling and Experiment of a New Axial-Type Superconducting Magnetic Bearing With Superconducting Coil. IEEE *Transactions on Applied Superconductivity*, **2024**, *34(5)*, pp. 1–10.
20. Rastogi, A.; Coombs, T.A.; Campbell, A.M.; Hall R. Axial Stiffness of Journal Bearings in Zero-Field and Field-Cooled Modes. IEEE Transactions on Applied Superconductivity, 2005, 15(2), pp. 1–3.
21. Peixoto, I.S.P.; da Silva, F.F.; Fernandes, J.F.P.; da Costa Branco, P.J. 3D Equivalent Space-Varying Permeability Model of HTS Bulks for Computation of Electromagnetic Forces. IEEE *Transactions on Applied Superconductivity*, **2021**, *31(5)*, pp. 1–7.
22. Hong, Z.; Campbell, H.M.; Coombs T.A. Computer Modeling of Magnetisation in High Temperature Superconductors. *IEEE Transactions on applied superconductivity*, **2007**, *17(2)*, pp. 3761- 3764.
23. Zhang, M.; Coombs, T.A. 3D modeling of high-Tc superconductors by finite element software. *IOP Superconductor Science and Technology*, **2012**, *25(1)*.